DESCRIPTION OF THE NORMAL HEAD STRUCTURES IN SHEEP (*OVIS ARIES*) BY MAGNETIC RESONANCE IMAGING AND ANATOMICAL CROSS-SECTIONS

TAHANY G.K. AHMED; ADAM, Z.E.; TAWFIEK, M.G. AND ABDEL MAKSOUD, M.K.M.

Department of Anatomy and Embryology, Faculty of Veterinary Medicine, Beni-Suef University, Beni-Suef 62511, Egypt.

ABSTRACT

The current study was designed to describe the normal structures of the head region in sheep using magnetic resonance imaging (MRI) and cross-sectional anatomy. Eight fresh heads of adult sheep of both sexes were used; two were scanned using MRI scanner with a 1.5 tesla magnet, and six fresh heads (n = 6) were frozen at -14°C to be sectioned into transverse (n = 4) and sagittal (n = 2) sections. The accessed MR images were serially matched to the corresponding gross sections for a comprehensive visualization of the relevant anatomical structures. The anatomical structures; bones, teeth, cartilages, muscles, membranes, nasal sinuses and meatuses exhibited variable intensities using T1- and T2-weighted MRI sequences. Moreover, the white and grey matter of the brain and cerebrospinal fluid were clearly outlined in T1- and T2-weighted MRI. The present study provided a normal anatomic reference of the head region of sheep using MRI to be used as a guide for further clinical diagnosis.

Key words: Cross-sectional Anatomy, Head, Magnetic Resonance Imaging (MRI), Sheep.

INTRODUCTION

Sheep is an important element of Egyptian agriculture income (30%). It occupies a progressive position in the Egyptian livestock section due to its suitability for the diverse agricultural conditions (Elshazly and Youngs, 2019).

There is a growing trend for application of ovine head models in medical and neuroscience research due to their large brain volume and clear neuro-anatomical structures (Boltze *et al.,* 2008). Recent diagnostic techniques such as radiography,

ultrasonography, computed tomography (CT) and magnetic resonance imaging (MRI) are useful tools for improving knowledge of the head anatomy (Penninck *et al.,* 2001). Using these modalities depends on the tissue being scanned (soft or hard tissue) and the hazard of ionizing radiation (Peterson *et al.,* 2017). Traditional radiography is insufficient for imaging soft tissues because of its low resolution and superimposition of bony features (Holmes, 2020). Ultrasonography is better for visualization of tendons and separate ligaments, while its non-invasive method cannot pass through bones and cartilages (Athar *et al.,* 2021). However, cross-sectional imaging modalities such as CT and MRI give an exceptional three-dimensional resolution for morphological and structural features (Holmes, 2020). Moreover, these

Corresponding author: Abdel Maksoud M.K.M.
E-mail address: mkamalvet@gmail.com
Present address: Department of Anatomy and Embryology, Faculty of Veterinary Medicine, Beni-Suef University, Beni-Suef 62511, Egypt.

techniques offer a clear visualization of the interior head and dental structures anatomy without superimposition of the complex skull bones (Mackey *et al.,* 2008). MRI is a reliable imaging modality that gives a great contrast to soft tissues by employing variety of imaging sequences (Thrall, 2013; Hagag and Tawfiek, 2018; Abdel Maksoud *et al.,* 2021). MRI technique is useful for normal anatomical and pathological studies due to its great soft-tissue contrast (Goncalves-Ferreira *et al.,* 2001; Arnold and Matthews, 2002). Moreover, it is considered the technique of choice for investigation of the central nervous system and extracranial soft tissues such as the orbit, muscles, salivary glands, blood vessels, and lymph nodes (Manso-Diaz *et al.,* 2015). It helps in the assessment of pathological conditions such as hemorrhage, tumors, inflammation, and chronic disorders (Cole and Hespel 2020). Many studies have been proposed to investigate the imaging appearance of the head structures using CT in Saanen goat (Tohidifar *et al.,* 2020), Ossimi sheep (Alsafy *et al*., 2020), and Ile de France sheep (Masoudifard *et al.,* 2022), and MRI in equines (Aref *et al.,* 2019), camel (Emam *et al.,* 2020). However, little literature is available for studying the normal sheep head structure using MRI. In consequence, this study aimed to use MRI and cross-anatomical sections for the characterization of the anatomical features of sheep head to be used as a reference for further clinical studies.

MATERIALS AND METHODS

Animals:

Eight heads of apparently healthy sheep (35-45kg body weight and 1-3 years old) were collected from the slaughterhouse in Beni-Suef province. To minimize postmortem alterations, the heads were removed from the level of the atlantoaxial joint, cleansed using tap water, and stored in an ice box at 4ºC to be scanned within 12 hrs. Two heads were used for MRI scanning, six heads were preserved frozen at -14ºC to be sectioned into four transverse and two sagittal sections. This study was approved by the Institutional Animal Care and Use Committee of Beni-Suef University, Egypt (BSU-IACUC-022-395, adopted on January 29, 2023).

MRI:

Two heads were used for MRI scanning. The heads were positioned with their longitudinal axes parallel to the examination stage using the human knee coil. Using a 1.5 Tesla multi-planar MRI magnet (Philips Intera, Holland), T1-weighted MR images were obtained with acquisitions; TR (repetition time) = 973msec, TE (echo delay time) = 15msec, FOV (field of view) = 220mm, slice thickness = 3.5mm, interstice space = 1mm). T2-weighted acquisitions; TR (repetition time) = 7318msec, TE (echo delay time) = 100msec, FOV (field of view) = 220/1.5mm, slice thickness = 3.5mm, interstice space =1mm). An automatic 3D reconstruction was applied for visualization of MR images into sagittal and transverse planes.

Cross Anatomical Sections:

The frozen heads (n=4) were sectioned using an electric saw into transverse and sagittal slices (2cm thickness). The selected slices were cleansed using tap water and a soft brush, and then photographed using a Samsung (WB-30F) digital camera.

Matching of Cross-anatomical Sections and MR images:

The obtained gross sections were clearly identified and serially numbered to be matched with their corresponding MR images. The anatomical terminology used in this investigation was consistent with Nomina Anatomica Veterinaria (2017).

RESULTS

Eight MR images and their corresponding gross sections were selected in matching to reference lines in Figure (1); seven in transverse planes (Figures 2-8) and one in a sagittal plane (Figure 9). For a better evaluation of the relevant anatomical

structures, the head region was divided into cranial, nasal, oral, orbital, and pharyngeal cavities.

Cranial cavity:
Bony parts of the cranial cavity included parietal, squamous part of the temporal, basilar part of the occipital, and basisphenoid bones were clearly outlined in transverse MR images. While parietal, pre-sphenoid, occipital and ethmoidal bones were delineated in sagittal MR images. These bony elements appeared hypointense in T1-weighted and with heterogeneous intermediate intensity in T2-weighted MR images (Figures 5-9). The brain tissue with its structural grey and white matter components, as well as the cerebrospinal fluid in the brain ventricles and subarachnoid spaces were depicted with variable intensities in different sequences of MRI. The white matter appeared with a low signal intensity in T2-weighted MRI (Figures 7, 9), and with an intermediate signal intensity in T1-weighted MRI (Figure 8). While, the grey matter was visualized with an intermediate signal intensity in T2-weighted MRI (Figures 7, 9), and with a high signal intensity in T1-weighted MRI (Figure 8). Moreover, the cerebrospinal fluid appeared with high signal intensity in T2-weighted MRI (Figures 7, 9), and with a low signal intensity in T1-weighted MRI (Figure 8). The transverse MRI images outlined the following parts of the brain; the crescent-shaped lateral ventricles, third ventricle, corpus callosum, hippocampus, thalamus, hypothalamus, and inter-thalamic adhesion (Figures 7, 8). While, the sagittal MR image delineated the following parts; olfactory bulb, cerebral hemisphere, cerebellum, lateral ventricle, inter-thalamic adhesion, pituitary gland, pons, and medulla oblongata (Figure 9).

Nasal cavity:
Bony boundaries of the nasal cavity were determined dorsally by the nasal bone, laterally by the maxilla, ventrally by the palatine process of the maxilla and vomer bone, and caudally by the cribriform plate of the ethmoidal bone. These bony parts appeared hypo-intense in T1-weighted MR images and with heterogonous intermediate intensity in T2-weighted MR images (Figures 2-7, 9). The nasal cavity was divided into two halves by a nasal septum which appeared with a homogenous intermediate intensity in both sequences of MRI (Figures 2-3, 4). This septum didn't reach the floor of the caudal part of the nasal cavity (Figures 5, 6). The nasal cavity is occupied by dorsal, middle, and ventral nasal conchae. The middle nasal concha was the shortest, and best evaluated in the sagittal image (Figure 9). In transverse images, the dorsal nasal concha scrolled ventrally to enclose the corresponding sinus. While the ventral one curved dorsally and ventrally to form the dorsal and ventral lamellae (Figures 2-3). Moreover, the sagittal image showed the rostral extension of the dorsal and ventral nasal conchae. The dorsal one is terminated by a straight fold (Figure 9) and the ventral one is terminated by basal and alar folds (Figure 9). These conchae were defined with intermediate intensities in both sequences of MRI (Figures 2-5, 9). The conchae divided the nasal cavity into dorsal, middle, and ventral nasal meatuses that appeared hypo-intense in both sequences of MRI (Figure 9). The dorsal and middle nasal meatuses were narrow and the ventral meatus was wide and directly lead to the choanae (Figure 9). Moreover, in the most rostral part of the nasal cavity, the vomeronasal organ was bilaterally situated on each side of the ventral part of the nasal septum and appeared hypo-intense in both sequences of transverse MRI (Figures 2-3).

The paranasal sinuses of sheep included; maxillary, frontal, lacrimal, sphenoidal, dorsal conchal, middle conchal, and ethmoidal. The maxillary sinus was incompletely divided by an infraorbital canal into medial and lateral chambers. The frontal sinuses were completely separated by inter frontal septum, each one was divided into three main groups of compartments; rostral, middle and caudal. The rostral compartment

of the frontal sinus was subdivided into three sub-compartments; medial, intermediate and lateral. The caudal frontal sinus also divided into nuchal and post-orbital compartments. Moreover, the lacrimal sinus appeared as a small excavation in the lacrimal bone. While, the sphenoidal sinus was a small cavity in the body and wing of sphenoid bone and extended to the wing of pre-sphenoid bone. However, the ethmoidal sinus appeared as a small space in the perpendicular plate of the ethmoidal bone. The dorsal and middle conchal sinuses occupied the cavity of the corresponding nasal conchae. These sinuses were depicted as hypo-intense structures in MRI sequences; transverse (Figures 3-7) and sagittal (Figure 9) images.

Oral cavity:

The lips, cheeks, hard palate, dental pad, and soft palate appeared with intermediate intensity in both sagittal and transverse MRI images (Figures 2-7, 9). The tough mucous membrane of the tongue appeared with higher intensity than the lingual muscles in both MRI sequences (Figures 2-6, 9). Moreover, the extrinsic lingual muscles appeared with an intermediate intensity in both sequences of transverse and sagittal MR images (Figures 3-6, 9). Dental structures of the oral cavity included; incisors (in sagittal), pre-molar and molar teeth (in transverse), were clearly identified as hypo-intense spaces in both sequences of MR images (Figures 4-5, 9). The cortical tissues of the mandible appeared hypo-intense. While its marrow cavity appeared hyper-intense in both MRI sequences (Figures 2-8). Osseous structures of the temporomandibular joint appeared hypo-intense and its adapting articular cartilage appeared with a heterogonous intermediate intensity in T2-weighted transverse MR images (Figure 8). The masticatory muscles; masseter, buccinator, temporalis, medial, and lateral pterygoid muscles were clearly outlined in transverse MR images (Figures 3-8). Moreover, facial muscles; inferior incisive, orbicularis oris, levator nasolabialis, and caninus were clearly

visualized in transverse MR images with intermediate intensities in both MRI sequences (Figure 2).

Orbital cavity:

Bony structures of the orbit were visualized with hypo-intensities in T1-weighted and heterogeneous intermediate intensity in T2-weighted MRI images (Figures 6-7). Chambers of the eyeball (anterior, posterior, and vitreous) were outlined with hypo-intense in T1-weighted and hyper-intense in T2-weighted MRI images (Figure 6-7). The anterior chamber was bounded rostrally by the cornea and appeared with intermediate intensity in T1-weighted and hypo-intense in T2-weighted MRI (Figures 6-7), and separated from the posterior chamber by the ciliary body and iris which appeared with intermediate intensity in T1-weighted MR images (Figure 6). The vitreous chamber was separated from the posterior one by the lens which could be evaluated with hypo-intense in T1-weighted MRI (Figure 6). The lens capsule was depicted as a hyper-intense narrow zone in T1-weighted MRI (Figure 6). The fibrous tunic of the eyeball including sclera and choroid could be visualized with hypo-intensity in T1-weighted and intermediate intensity in T2-weighted MRI (Figures 6-7). Otherwise, the retina couldn't be identified from the choroid as they had the same intensity.

The extraocular muscles; medial rectus, dorsal rectus, ventral rectus, lateral rectus and retractor bulbi muscles were outlined with intermediate intensities in both sequences of MRI, the orbital fat surrounded the eyeball and muscles appeared hyper-intense in T2-weighted MRI. The eyelids (upper, lower, and third) appeared with intermediate intensities in T1-weighted MRI, the lacrimal gland appeared hyper-intense in T1-weighted and a homogenous intense in T2-weighted MRI (Figures 6-7).

Pharyngeal cavity:

The pharyngeal cavity was incompletely divided by the soft palate into dorsal nasopharynx and ventral oropharynx. The

oropharynx appeared with intermediate intensity in T2-weighted MRI (Figure 9). The nasopharynx led to the larynx which consisted of cartilages; epiglottis, thyroid, corniculate, cricoid, arytenoid, these cartilages appeared with slightly hyper-intensities in both sequences of MRI (Figures 7-9). Furthermore, muscles of the larynx; thyro-arytenoid, hyo-epiglottic, geniohyoid, mylohyoid, thyrohyoid, omohyoid, and sternohyoid were defined with intermediate intensities in both sequences of MRI (Figures 2-7, 9). The basihyoid, thyrohyoid, styloid process, and lingual process of the hyoid bone were clearly depicted with hypo-intensities in T1-weighted and heterogeneous intermediate intensities in T2-weighted MRI (Figures 6, 9). Moreover, the vocal folds were detected with intermediate intensity in T1-weighted MR images (Figure 8).

Legends of figures
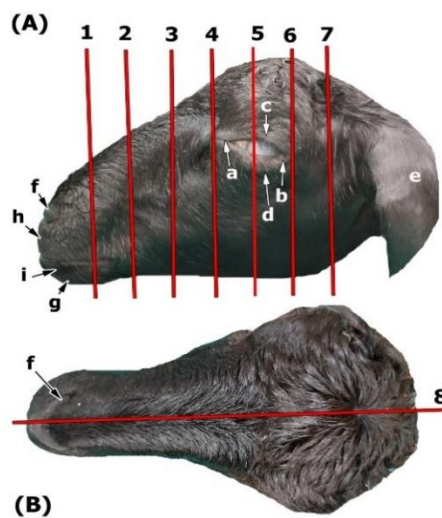
Figure 1: Lateral aspect of the sheep head (A) and dorsal aspect (B). The numbered red lines indicated the selected planes of each anatomical section and MRI; transverse planes (1-7) and sagittal plane (8). Medial canthus (a), lateral canthus (b), upper eyelid (c), lower eyelid (d), external ear (e), nostril (f), chin (g), upper lip (h), lower lip (i).
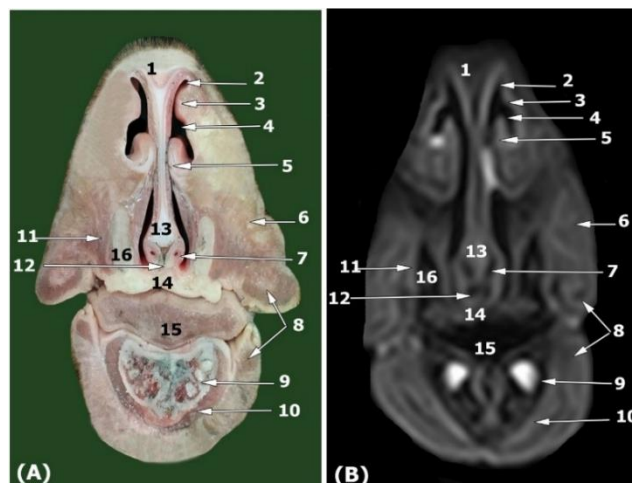
Figure 2: Transverse section of the sheep head (plane 1 as designated in Figure 1): Anatomical section (A) and T2-weighted magnetic resonance image (B). Nasal bone (1), dorsal nasal meatus (2), straight fold of dorsal nasal concha (3), middle nasal meatus (4), alar fold of ventral nasal concha (5), levator nasolabialis muscle (6), vomeronasal organ (7), orbicularis oris muscle (8), body of mandible (9), inferior (mandibular) incisive muscle (10), caninus muscle (11), vomer bone (12), nasal septum (13), hard palate (14), body of tongue (15), nasal process of incisive bone (16).
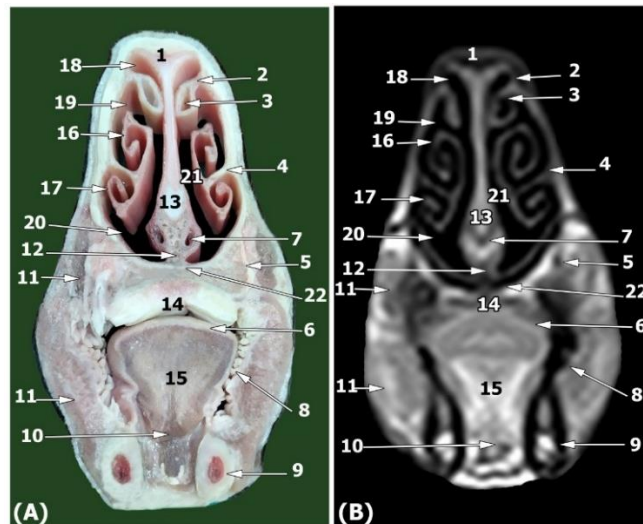
Figure 3: Transverse section of sheep head (plane 2 as designated in figure 1): anatomical section (A) and T1-weighted magnetic resonance image (B). Nasal bone (1), Dorsal nasal concha (2), dorsal nasal sinus (3), ventral nasal concha (4), maxilla (5), tunica mucosa of tongue (6), vomeronasal organ (7), mucosa of cheek (8), body of mandible (9), genioglossus muscle (10), buccinator muscle (11), vomer bone (12), nasal septum (13), hard palate (14), body of tongue (15), dorsal spiral lamellae of the ventral nasal concha (16), ventral spiral lamellae of the ventral nasal concha (17), dorsal nasal meatus (18), middle nasal meatus (19), ventral nasal meatus (20), common nasal meatus (21), palatine process of maxilla (22).
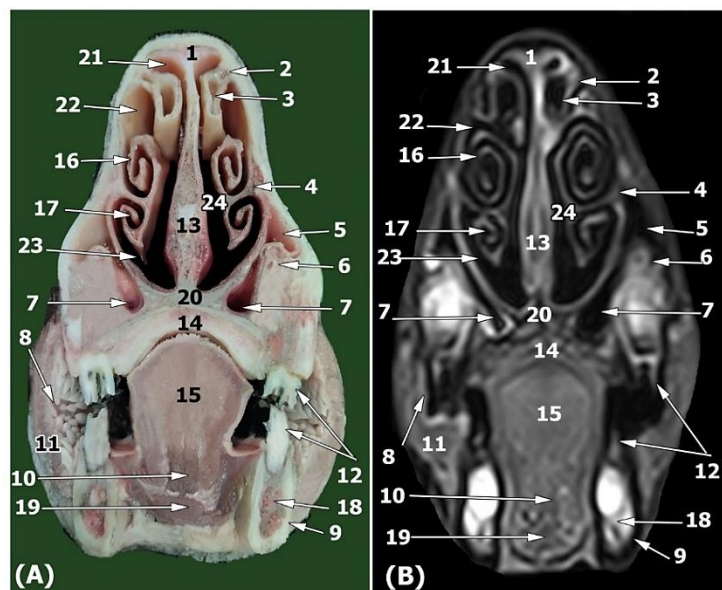
Figure 4: Transverse section of sheep head (plane 3 as designated in figure 1): anatomical section (A) and T2-weighted magnetic resonance image (B). Nasal bone (1), dorsal nasal concha (2), dorsal nasal sinus (3), ventral nasal concha (4), lateral chamber of maxillary sinus (5), infraorbital canal (6), medial chamber of maxillary sinus (7), mucosa of the cheek (8), mandible (cortical tissue of the body) (9), genioglossus muscle (10), buccinators muscle (11), dorsal and ventral second pre-molar teeth (12), nasal septum (13), hard palate (14), body of tongue (15), dorsal spiral lamellae of the ventral nasal concha (16), ventral spiral lamellae of the ventral nasal concha (17), bone marrow of mandible (18), geniohyoideus muscle (19), palatine process of maxilla (20), dorsal nasal meatus (21), middle nasal meatus (22), ventral nasal meatus (23), common nasal meatus (24).
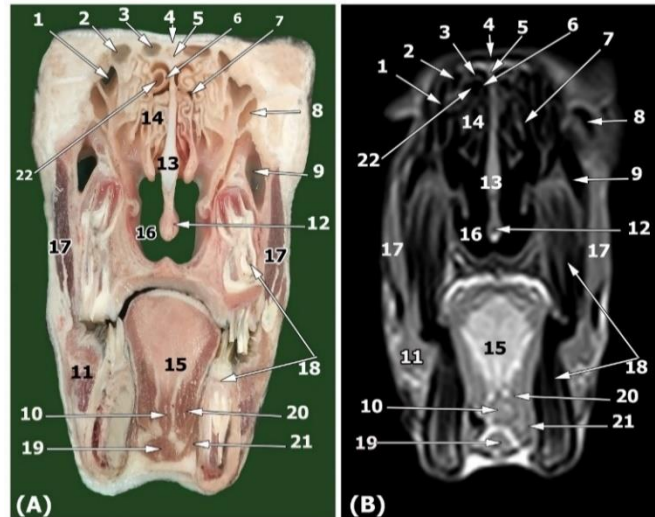
Figure 5: Transverse section of sheep head (plane 4 as designated in figure 1): anatomical section (A) and T1-weighted magnetic resonance image (B). Lateral compartment of rostral frontal sinus (1), intermediate compartment of rostral frontal sinus (2), medial compartment of rostral frontal sinus (3), frontal bone (4), inter-frontal septum (5), middle nasal concha (6), ethmoidal sinus (7), lacrimal sinus (8), lacrimal bulla (9), genioglossus muscle (10), buccinator muscle (11), vomer bone (12), nasal septum (13), ethmoidal labyrinth (14), body of tongue (15), choanae (16), masseter muscle (17), dorsal and ventral third molar teeth (18), geniohyoideus muscle (19), hyoglossus muscle (20), mylohyoideus muscle (21), middle conchal sinus (22).
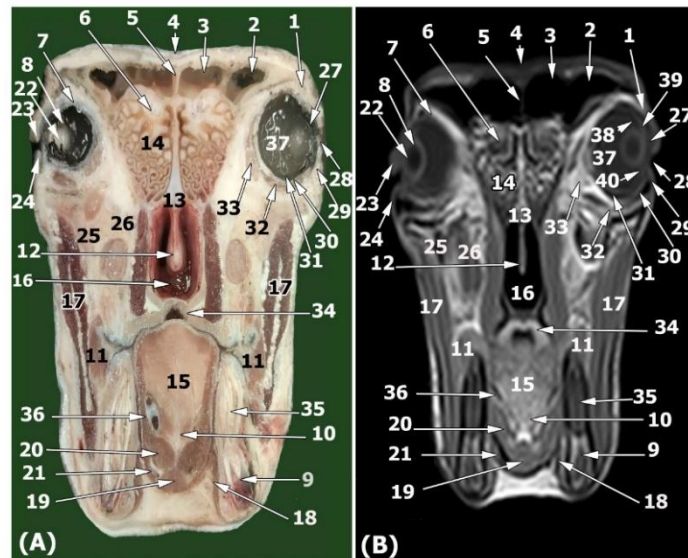
Figure 6: Transverse section of sheep head (plane 5 as designated in figure 1): anatomical section (A) and T1-weighted magnetic resonance image (B). Lacrimal gland (1), post orbital diverticulum of the caudal group of compartments of frontal sinus (2), middle group of compartments of frontal sinus (3), frontal bone (4), inter-frontal septum (5), ethmoidal fossa (6), external lamina of frontal sinus (7), lens capsule (8), body of mandible (9), genioglossus muscle (10), buccinator muscle (11), vomer bone (12), nasal septum (13), ethmoidal labyrinth (14), tongue (15), choanae (16), masseter muscle (17), medial pterygoid muscle (18), geniohyoideus muscle (19), hyoglossus muscle (20), mylohyoideus muscle (21), lens (22), upper eyelid (23), lower eyelid (24), zygomatic bone (25), lacrimal bone (26), aqueous humor (27), cornea (28), third eyelid (29), sclera (30), choroid (31), medial rectus muscle (32), retractor bulbi muscle (33), soft palate (34), root of last molar teeth (35), lingual process of hyoid bone (36), vitreous chamber (37), posterior chamber (38), ciliary body (39), iris (40).
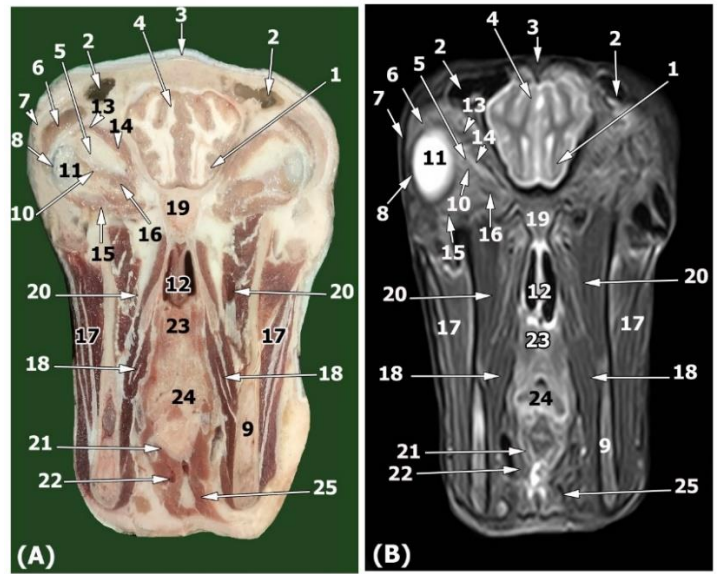
Figure 7: Transverse section of sheep head (plane 6 as designated in figure 1): anatomical section (A) and T2-weighted magnetic resonance image (B). Cerebral gray matter (1), nuchal diverticulum of the caudal group of compartment of frontal sinus (2), parietal bone (3), cerebral white matter (4), peri-orbital fat (5), lacrimal gland (6), zygomatic arch (7), sclera (8), ramus of the mandible (9), retractor bulbi muscle (10), vitreous chamber (11), vomer bone (12), dorsal rectus muscle (13), medial rectus muscle (14), lateral rectus muscle (15), ventral rectus muscle (16), masseter muscle (17), medial pterygoid muscle (18), basisphenoid bone (19), lateral pterygoid muscle (20), thyroid cartilage (21), thyrohyoideus muscles (22), soft palate (23), epiglottis (24), omohyoideus and sternohyoideus muscles (25).
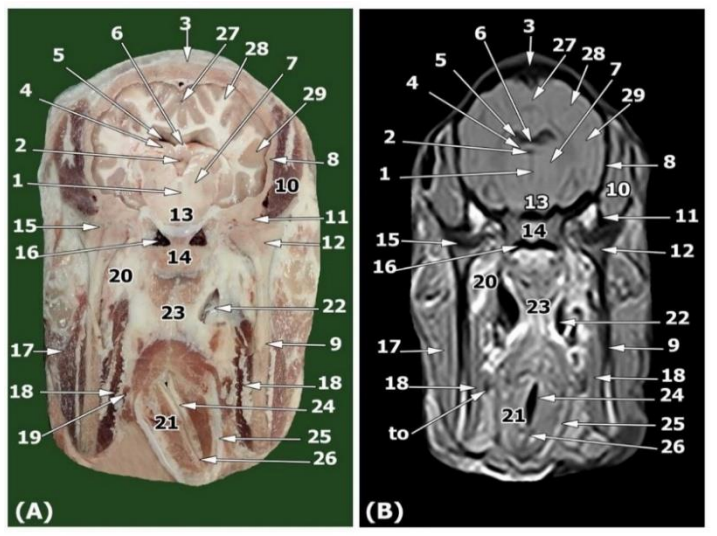
Figure 8: Transverse section of sheep head (plane 7 as designated in figure 1): anatomical section (A) and T1-weighted magnetic resonance image (B). Inter-thalamic adhesion (1), third ventricle (2), parietal bone (3), hippocampus (4), lateral ventricle (5), corpus callosum (6), thalamus (7), squamous part of temporal (8), ramus of the mandible (9), temporalis muscle (10), the articular process of the temporal bone (11), the condylar process of the mandible (12), hypothalamus (13), basilar part of the occipital bone (14), articular cartilage of temporomandibular joint (15), cavernous venous sinus (16), masseter muscle (17), pterygoid muscle (medial part) (18), thyrohoid bone (19), lateral pterygoid muscle (20), tyro-arytenoid muscle (21), styloid process of hyoid bone (22), soft palate (23), arytenoid cartilage (24), thyroid cartilage (25), vocal fold (26), cerebral longitudinal fissure (27), cerebral white matter (28), cerebral gray matter (29).

71
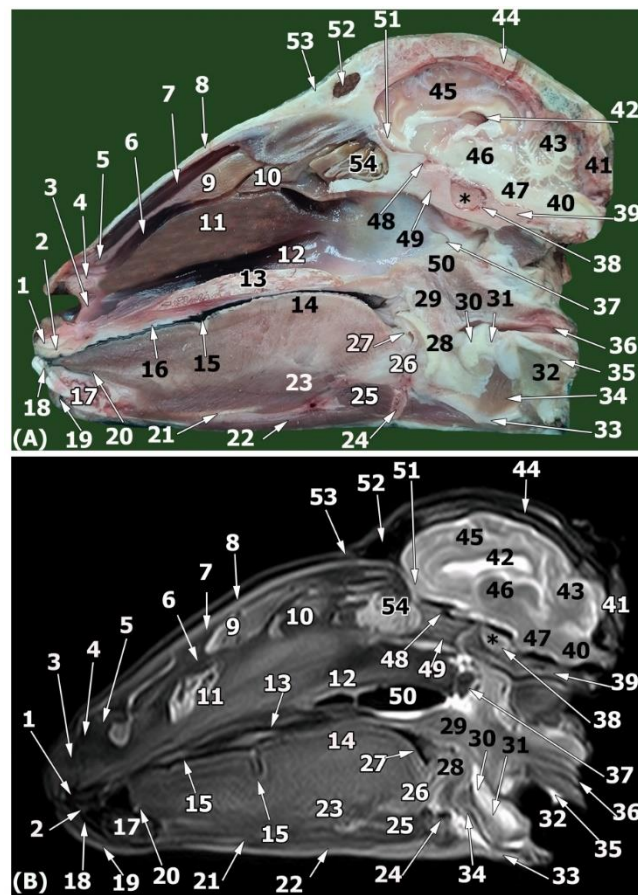
Figure 9: Sagittal section of sheep head (plane 8 as designated in figure 1): anatomical section (A) and T2-weighted magnetic resonance image (B). Palatine process of incisive bone (1), dental pad (2), basal fold (3), alar fold (4), straight fold (5), middle nasal meatus (6), dorsal nasal meatus (7), nasal bone (8), dorsal nasal concha(9), middle nasal concha (10), ventral nasal concha (11), ventral nasal meatus (12), palatine process of maxilla (13), torus linguae (14), fossa linguae (15), hard palate (16), body of the mandible (17), incisor teeth (18), lower lip (19), genioglossus muscle (20), geniohyoideus muscle (21), mylohyoideus (22), styloglossus (23), basihyoid bone (24), hyoglossus muscle (25), hyo-epiglottic muscle (26), oropharynx (27), epiglottis (28), soft palate (29), corniculate cartilage (30), arytenoid cartilage (31), laryngeal cavity (32), thyroid cartilage (33), thyroarytenoid muscle (34), cricoid cartilage (35), esophagus (36), internal acoustic meatus (37), hypophyseal fossa (38), basisphenoid bone (39), medulla oblongata (40), occipital bone (41), lateral ventricle (42), cerebellum (43), parietal bone (44), cerebrum (45), inter-thalamic adhesion (46), pons (47), sphenoid sinus (48), pre-sphenoid bone (49), nasopharynx (50), olfactory bulb (51), frontal sinus (52), frontal bone (53), ethmoidal labyrinth (54), pituitary gland (*).

DISCUSSION

The present study provided an accurate reference of MR images of the normal sheep head region based on their corresponding anatomical cross-sections. MR images provided illustration of the cranial, nasal, pharyngeal, orbital cavities and all structures of the head in three-dimensional planes and sequent slices that allow the clinicians to recognize these structures and help in the diagnosis of any disorders of the sheep head structures.

Using MR images with their corresponding anatomical cross-sections in this study provided excellent visualization and discrimination of the head region's soft and hard tissue structures. Hence, the MRI was considered a useful diagnostic tool for distinct discrimination of the soft tissue from that rich with mineral and gas-

containing sacs especially in complex-structured regions (Arencibia *et al.,* 2000; Pease *et al.,* 2017). In the present study, we used T1 and T2-weighted sequences of MRI for a good delineation of different structures. In this respect, T2-weighted images provide a better contrast between white and grey matter and cerebrospinal fluid than T1-weighted MRI (Kassab, 2011, Abdel Maksoud *et al.,* 2021).

Paranasal sinuses of the sheep; dorsal and middle conchal sinus, maxillary, frontal, lacrimal, sphenoidal, and ethmoidal sinuses were observed (Awaad *et al.,* 2019, Alsafy *et al.,* 2020; Masoudifard *et al.,* 2022). Whereas the ventral conchal sinus was difficult to notice in sheep which might attributed to the presence of spiral lamellae in ventral nasal concha (Awaad *et al.,* 2019; Masoudifard *et al.,* 2022). Otherwise, the ventral conchal sinus was observed in horse (Budras *et al.,* 2003, Aref *et al.,* 2019). Furthermore, the palatine sinus couldn't be visualized in sheep (Awaad *et al.,* 2019), even though, it was observed in sheep (May, 1970; Sisson, 1975) and goat (Kareem and Sawad, 2016).

The current study provided a good visualization of the orbital cavity, ocular structures, chambers, and orbital relationships. Understanding these anatomical structures could help in the diagnosis of ophthalmic diseases and early detection of intracranial extension (Kono *et al.,* 2002; Aviv and Casselman 2005), as well as protection from any injuries that might occur during the application of the orbital devices (Michau and Gilger 2004). Moreover, using the MRI admitted a clear visualization of bony boundaries and deep structures of the orbital cavity, which might help in the evaluation of the bony rim invasion (Davis *et al.,* 2002; Goh *et al.,* 2008). Moreover, topographic investigation of the orbit in this study showed its relation to the paranasal sinuses, this topographic relation could explain the extension of the paranasal

sinuses infection to the orbit (Rootman, 2002). Chambers of the eye were detected with high signal intensity in T2-weighted MRI and low signal intensity in T1-weighted MRI (Awaad *et al.,* 2022). Otherwise, it was difficult to outline the retina using MRI (Aviv and Casselman, 2005; Goh *et al.,* 2008; D'Aout *et al.,* 2014; Awaad *et al.,* 2022), Furthermore, the sclera was clearly differentiated from the choroid using MRI (Awaad *et al.,* 2022). However, the ocular structures, sclera and choroid, couldn't be differentiated by Reef (1998) and D'Aout *et al.* (2014).

CONCLUSION

The present study provided an excellent anatomic reference of the sheep head region using cross-sectional anatomy and MRI to help veterinary clinicians in the clinical diagnosis and interpretation of this region in sheep.

CONFLICT OF INTEREST

The authors declare that no conflict of interest.

REFERENCES

Abdel Maksoud, MKM.; Halfaya, FM.; Mahmoud, HH. and Ibrahim, AAH. (2021): Morphological characteristics of the forebrain in the donkey Equus asinus: A compared atlas of magnetic resonance imaging and cross-sectional anatomy. Anatomia Histologia Embryologia, 50:974-984. https://doi.org/10.1111/ahe.12744

Alsafy, M.; Madkour, N.; Abumanolour, M.; El-Gendy, S. and Kalkpura, A. (2020): Anatomical description of the head in ossimi sheep: sectional anatomy and computed tomographic approach. Morphologie, 105(348): 29-44. https:// doi.org /10.10161 j.morpho.2020.06.008

Aref, M.; Ismail, A.A.; Emam, H. and Dhama, K. (2019): Identification of normal horse head structures, with special reference to paranasal sinuses, by anatomical cross-section and magnetic resonance imaging (MRI). Adv. Anim. Vet. Sci., 7(3):200-204. https://doi.org /10.17 582/Journal.aavs/2019/7.3.200.204.

Arencibia, A.; Vazquez, JM.; Jaber, R.; Gil, F.; Ramirez, JA.; Rivero, M.; Gonzalez, N. and Wisner, ER. (2000): Magnetic resonance imaging and cross sectional anatomy of the normal equine sinuses and nasal passages. Vet. Radiol. Ultrasound, 41(4): 313-319. https://doi.org/ 10.1111/j.1740-8261.2000.tb02079.x

Arnold, D.L. and Matthews, P.M. (2002): MRI in the diagnosis and management of multiple sclerosis. Neurol., 58: 23-31. https://doi.org 10.1212/wnl.58.8_suppl_4.s23

Athar, H.; Parrah, JD.; Mir, AQ.; Moulvi, BA.; Makhdoomi, DM.; Dar, MU. and Handoo, N. (2021): Ocular ultrasonography and echobiometry in goats of different age and breed. Indian Journal of Animal Research, B-4360:1-5. https://doi.org/10.18805 /IJAR.B-4360

Aviv, RI. and Casselman. J. (2005): Orbital imaging: Part 1 Normal anatomy. Clinical Radiology, 60: 279-287. https://doi.org/ 10.1016/j.crad.2004. 05.017

Awaad, AS.; Abdel Maksoud, MKM. and Fathi, MZ. (2019): Surgical anatomy of the nasal and paranasal sinuses in Egyptian native sheep Ovis aries using computed tomography and cross sectioning. Anatomia Histologia Embryologia, 48:279-289. https://doi.org/10.1111/ahe.12436

Awaad, AS.; Halfaya, FM.; Ibrahim, AAH. and Abdel Maksoud, M.K.M. (2022): Magnetic resonance imaging and cross-sectional anatomy of the eye and the optic nerve in the Egyptian donkey (*Equus asinus*). International Journal of Veterinary Science,

11(4):526-532. https://doi.org/10. 47278/journal.ijvs/2022.141

Boltze, J.; Förschler, A.; Nitzsche, B.; Waldmin, D.; Hoffmann, A.; Boltze, CM.; Dreyer, A.Y.; Goldammer, A.; Reischauer, A.; Hartig, W.; Geiger, D.K.; Barthel, H.; Emmrich, F. and Gille, U. (2008): Permanent middle cerebral artery occlusion in sheep: a novel large animal model of focal cerebral ischemia. J Cereb Blood Flow Metab, 28(12):1951–1964. https://doi.org/10.1038/jcbfm.2008.8 9

Budras, K.D.; Habel, R.E.; Wunsche, A. and Buda, S. (2003): Bovine anatomy, an illustrated text. 1st ed. Hannover, Germany, Schlutersche Gmbh. Pp. 44-45.

Cole, R. and Hespel, A.M. (2020): Principles of computed tomography and magnetic resonance imaging. In: M. Holland, and J. Hudson (Eds.), Feline diagnostic imaging. Wiley Blackwell publication (pp. 13-26). https://doi.org/10.1002/97811188409 31.ch2

D'Aout, C.; Nisolle, JF.; Navez, M.; Perrin, R.; Launois, T.; Brogniez, L.; Clegg, P.; Vandeweerd, JM. and Hontoir, F. (2014): Computed tomography and magnetic resonance anatomy of the normal orbit and eye of the horse, Anatomia Histologia Embryologia, 445: 370-377. https://doi.org/10.1111/ahe.12149

Davis, JL.; Gilger, BC.; Spaulding, K.; Robertson, ID. and Jones, SL. (2002): Nasal adenocarcinoma with diffuse metastases involving the orbit, cerebrum, and multiple cranial nerves in a horse. Journal of American Veterinary Medical Association, 221:1460–1463. https://doi: 10.2460/javma.2002.221. 1460

Elshazly, A.G. and Youngs, C.R. (2019): Feasibility of utilizing advanced reproductive technologies for sheep breeding in Egypt. Part1. Genetic

and nutritional resources. Egyptian Journal of Sheep & Goat Sciences, 14(1):39-52. http://doi.org/10.21608/EJSGS.2019.33235

Emam, H.; Aref, M.; Ismail, A.A.; Abdelaal, A.; Gouda, S. and Gommaa, M. (2020): Description of normal head structures of the one-humped camel (camelus dromedaries) by magnetic resonance imaging, computed tomography, and cross-sectional anatomy. Veterinary world, 13(8):1581-1587. http://doi.org/14202/vet word.2020.1581-1587

Goh, PS.; Gi, MT.; Charlton, A.; Tan, C.; Gangadhara Sundar, JK. and Amrith, S. (2008): Review of orbital imaging. European Journal of Radiology, 66:387–395. http://doi.org/10.1016/ j.ejrad.2008.03.031

Goncalves-Ferreira, A.J.; Herculano-Carvalho, M.; Melanicia, J.P.; Farias, J.P. and Gomes, L. (2001): Corpus Callosum: microsurgical anatomy and MRI. Surg. Radiol. Anat., 23:409-414. http://doi.org 10.1007/s00276-001-0409-z

Hagag, U. and Tawfiek, M.G. (2018): Ultrasonography, computed tomography and magnetic resonance imaging of bovine metacarpo/metatarsophalangeal joint. The Veterinary Journal, 233:66-75. https://doi.org/10.1016/j.tvjl.2018.01.001.

Holmes, S.P. (2020): Diagnostic imaging of diseases of the skull. In: M. Holland, & J. Hudson (Eds.), Feline diagnostic imaging. Wiley Blackwell publication (pp.47-75).

Kareem, D.A. and Sawad, A.A. (2016): Silicon polymer for cast of paranasal sinuses of Iraqi local goat (*Capra hircus*). Basrah Journal of Veterinary Research, 15(1):111–118. DOI: 10.33762/bvetr.2016.124260

Kassab, A. (2011): Magnetic resonance image and cross-sectional anatomy of the normal brain of goat (*Capra hircus*). Emirates Journal of Food and Agriculture, 23(4):375-380.

Kono, R.; Poukens, V. and Demer, JL. (2002): Quantitative analysis of the structure of the human extraocular muscle pulley system. Investigative Ophthalmology and Visual Science, 43:2923–2932.

Mackey, E.B.; Divers, S.J.; Holland, M. and Frank, P. (2008): Clinical technique: Application of computed tomography in zoological medicine. Journal of Exotic Pet Medicine,. 17(3):198-209. https://doi.org/10.1053/j.jepm.2008.05.007

Manso-Diaz, G.; Dyson, SJ.; Dennis, R.; Garcia-Lopez, JM.; Biggi, M.; Garcia-Real, MI.; San Roman, F. and Taeymans, O. (2015): Magnetic resonance imaging characteristics of equine head disorders: 84 cases (2000-2013). Vet. Radiol. Ultrasound, 56(2):176-187. http://doi.org/10.1111/vru.12210

Masoudifard, M.; Zehtabvar, O.; Modarres, S.H.; Pariz, F. and Tohidifar, M. (2022): CT anatomy of the head in the ille de France sheep. Veterinary Medicine and Science, 8:1694-1708. https:// doi.org/ 10.1002/vms3.834

May, N.D.S. (1971): The anatomy of the sheep. 3rd ed. Brisbane, Australia, University of Queensland press. Pp. 171-175.

Michau, TM. and Gilger, BC. (2004): Cosmetic globe surgery in the horse. Veterinary Clinics of North America: Equine Practice, 20:467–484. https://doi.org/10.1016/j.cveq.2004.04.001

Nomina Anatomica Veterinaria (2017): International Committeeon Veterinary Gross Anatomical Nomenclature and authorized by the general assembly of the World Association of Veterinary Anatomist 6th ed.: Germany:ICVGAN.

Pease, A.; Mair, T. and Spriet, M. (2017): Imaging the equine head and spine.

Equine Vet. J., 49(1):13-14. https://doi.org/10.1111/evj.12640

Penninck, D.; Daniel, GB.; Brawer, R. and Tidwell, AS. (2001): Cross sectional imaging techniques in veterinary ophthalmology. Clinical Techniques in Small Animal Practice, 16: 22–39. https:// doi.org/10.1053/svms. 2001. 22802

Peterson, N.; Widnall, J.; Evans, P.; Jackson, G. and Platt, S. (2017): Diagnostic imaging of diabetic foot disorders. Foot & Ankle International, 38(1): 86-95. https://doi.org/10.1177/1071100716672660

Rootman, J. (2002): Distribution and differential diagnosis of orbital disease. In: Diseases of the orbit: a multidisciplinary approach. 2ed ed. Philadelphia, PA: Lippincott, Williams and Wilkins, 52-84.

Reef, VB. (1998): Ultrasonographic evaluation of small parts. In: Equine diagnostic ultrasound. Reef VB ed, Philadelphia: WB Saunders.480–547.

Sisson, S. (1975): Ruminant osteology. In R. Getty (Ed.), The anatomy of the domestic animals, 5th ed. Philadelphia, USA, W.B. Saunders, (pp. 785–786).

Thrall, DE. (2013): Textbook of veterinary diagnostic radiology. 6th Ed. Elsevier Saunders, Missouri: USA, pp: 50-55.

Tohidifar, M.; Goodarzi, N. and Masoudifard, M. (2020): Anatomy of the head in the saanen goat: a computed tomographic and cross-sectional approach. Anatomical Science International, 95:408-419. https://doi.org/10.1007/s1256-020-00536-0

وصف التراكيب الطبيعية لرأس الأغنام (*Ovis aries*) باستخدام التصوير بالرنين المغناطيسي والتشريح المقطعي

تهانى جمال قرنى أحمد ، زين العابدين عبد الستار آدام ، محمد جمعة توفيق محمد كمال مرعى عبدالمقصود

Email: mkamalvet@gmail.com   Web-site: www.aun.edu.eg

استهدفت الدراسة الحالية توصيف التراكيب الطبيعية لمنطقة الرأس فى الأغنام عن طريق التصوير بأشعة الرنين المغناطيسي وبتوصيف التشريح المقطعي. تم استخدام ثمانية رؤوس طازجة لأغنام بالغة من كلا الجنسين. تم فحص اثنين منها باستخدام ماسح التصوير بالرنين المغناطيسي (١,٥ تسلا)، وتم تجميد ستة رؤوس عند ١٤- درجة مئوية لتقطيعها إلى مقاطع عرضية (أربعة رؤوس) وسهمية (رأسان). تمت مطابقة صور الرنين المغناطيسي التي تم الوصول إليها بشكل تسلسلي مع المقاطع التشريحية المقابلة مما يوفر رؤية شاملة للتراكيب التشريحية ذات الصلة. أظهرت التراكيب التشريحية: العظام والأسنان والغضاريف والعضلات والأغشية والجيوب الأنفية والممرات الأنفية كثافة متغيرة باستخدام متواليين من أشعة الرنين المغناطيسي (T1- and T2-weighted). وعلاوة على ذلك ، تم تحديد المادة البيضاء والرمادية من أنسجة المخ والسائل النخاعي الشوكي بشكل واضح في التصوير بالرنين المغناطيسي (T1- and T2-weighted). قدمت الدراسة الحالية مرجعًا تشريحيًا طبيعيًا لمنطقة الرأس فى الأغنام باستخدام التصوير بالرنين المغناطيسي لاستخدامه فى التشخيص السريري.